Journal of
Sensor and Actuator Networks

MDPI

Article

AI Correction of Smartphone Thermal Images: Application to Diabetic Plantar Foot

Hafid Elfahimi [1,*], Rachid Harba [2,*], Asma Aferhane [1], Hassan Douzi [1] and Ikram Damoune [3]

[1] IRF-SIC Laboratory, Ibn Zohr University, Agadir 80000, Morocco; asma.aferhane@edu.uiz.ac.ma (A.A.); h.douzi@uiz.ac.ma (H.D.)
[2] PRISME Laboratory, Orléans University, 45072 Orléans, France
[3] Faculty of Medicine and Pharmacy, Ibn Zohr University, Agadir 80000, Morocco
* Correspondence: hafid.elfahimi.37@edu.uiz.ac.ma (H.E.); rachid.harba@univ-orleans.fr (R.H.)

Abstract

Prevention of complications related to diabetic foot (DF) can now be performed using smartphone-connected thermal cameras. However, the absolute error associated with these devices remains particularly high, compromising measurement reliability, especially under variable environmental conditions. To address this, we introduce a physiologically motivated two-region segmentation task (forehead + plantar foot) to enable stable temperature correction. First, we developed a fully automated joint method for this task, building upon a new multimodal thermal–RGB dataset constructed with detailed annotation procedures. Five deep learning methods (U-Net, U-Net++, SegNet, DE-ResUnet, and DE-ResUnet++) were evaluated and compared to traditional baselines (Adaptive Thresholding and Region Growing), demonstrating the clear advantage of data-driven approaches. The best performance was achieved by the DE-ResUnet++ architecture (Dice score: 98.46%). Second, we validated the correction approach through a clinical study. Results showed that the variance of corrected temperatures was reduced by half compared to absolute values ($p < 0.01$), highlighting the effectiveness of the correction approach. Furthermore, corrected temperatures successfully distinguished DF patients from healthy controls ($p < 0.01$), unlike absolute temperatures. These findings suggest that our approach could enhance the performance of smartphone-connected thermal devices and contribute to the early prevention of DF complications.

Keywords: diabetic foot; thermal images; deep learning; segmentation; mobile health

Check for updates

Academic Editors: Chengwen Luo, Xingyu Feng and Chao Fan

Received: 26 November 2025
Revised: 15 January 2026
Accepted: 19 January 2026
Published: 26 January 2026

Copyright: © 2026 by the authors. Licensee MDPI, Basel, Switzerland. This article is an open access article distributed under the terms and conditions of the Creative Commons Attribution (CC BY) license.

1. Introduction

Patients with diabetes mellitus are exposed to a range of complications that notably affect the feet, eyes, kidneys, and cardiovascular and nervous systems [1,2]. Of these, diabetic foot (DF) is of particular interest. According to standard definitions, this nosological entity encompasses lesions such as infections, ulcerations, and deep tissue destruction, which are often associated with peripheral neuropathy and lower limb arteriopathy [3,4].

Clinical management of DF disease generates considerable human and economic costs. Ulceration and amputation represent the most severe complications [5], profoundly affecting patients' quality of life and placing a significant burden on healthcare systems [6]. Given the progressive nature of this condition, early detection of complications is a major clinical challenge.

Infrared thermography is widely employed in diverse fields such as space exploration, civil engineering, and medicine. Characterized by its non-invasiveness, operational safety,

and technical accessibility, it has established itself as a reliable methodology with broad interdisciplinary applicability. In the case of DF disease, this technique has demonstrated a notable effectiveness in identifying ulcer-prone regions. According to studies [7,8], thermal monitoring of plantar foot in DF patients can reduce the incidence of ulcers by 70%. This major finding clearly indicates the critical importance of investigating plantar thermal variations in greater depth and developing novel strategies to better understand the underlying pathophysiological mechanisms and optimize clinical monitoring protocols.

In this context, several approaches have been developed. Independent foot analysis examines each foot separately to identify local thermal anomalies. Study [9] explored the correlation between the temperature of specific zones and foot deformities. Another approach, based on the idea of contralateral symmetry, analyzes the temperature differences between the two feet, as any asymmetry can indicate an anomaly. Studies [10,11] have shown that this technique enables the identification of ulcerous areas by superimposing the feet for direct comparison. Furthermore, analysis of regional temperature distribution in the plantar foot has been employed, as in study [12], which proposed classifying patients according to their ulcer risk based on the angiosome concept. Finally, the thermal stress approach relies on external stimulation techniques, such as the cold stress test, which investigates vascular and thermoregulatory dysfunctions in DF patients. Studies [13,14] have shown that the cold stress test is a promising method for early diabetic neuropathy diagnosis.

Recently, with scientific and technological advancements, temperature monitoring for the early detection of DF complications using thermal cameras connected to smartphones has generated increasing interest. However, these cameras are subject to significant absolute errors caused by material and environmental factors. In this context, devices such as FLIR One Pro cameras [15], HIMICRO Mini1 [16], UNI-T UTI721M [17], and TOPDON TC001 [18] exhibit absolute errors no better than ±2 °C. This margin of error can affect the accuracy of the measurement and compromise the interpretation of the data for diagnostic purposes. This issue becomes particularly critical under variable environmental conditions.

To address these limitations, this study proposes an innovative and fully automated method that incorporates an original thermal correction strategy using forehead temperature as a physiological thermal reference. The forehead was selected as a reference site for several reasons. Previous thermographic studies have reported the forehead as a stable and reliable anatomical region for temperature assessment, commonly used as a reference area in medical infrared thermography [19,20]. The forehead is also practically accessible during clinical examinations, as our acquisition protocol simultaneously captures thermal images of both feet and the forehead without requiring additional patient manipulation. Furthermore, it is particularly suitable for DF patients: while these complications primarily affect the lower extremities, facial vasculature is generally preserved, providing a stable internal thermal baseline for temperature correction. We propose a novel joint segmentation that associates thermal and RGB images of both feet and the forehead. This methodological approach significantly reduces the absolute error of the camera and improves the reliability of thermal analysis. The experimental results show a significant reduction in thermal variance after correction and reveal a significant discriminatory capacity between DF patients and healthy controls, thus validating the clinical potential of the method for the early detection of DF complications.

This article is structured as follows: Section 2 presents the materials and protocol used for image acquisition, as well as the methods used for joint segmentation of both feet and forehead. Section 3 details the dataset and the comparative results of the segmentation methods. Section 4 presents the transversal clinical study involving DF patients and healthy controls. Finally, a discussion and conclusion are provided in the Sections 5 and 6.

2. Materials and Methods

2.1. Data Acquisition

2.1.1. Materials

The acquisition of images was carried out with a FLIR ONE Pro thermal camera (Berlin Germany) connected to a Samsung Galaxy S8 smartphone (Thai Nguyen, Vietnam). This device features a thermal resolution of 160 × 120 pixels and operates within a spectral range of 8–14 µm. With an absolute error of ±3 °C, it is capable of simultaneously capturing both thermal and RGB images, which are spatially calibrated to enhance measurement accuracy. Figure 1 shows an example of acquired images.



Figure 1. Acquisition example: (***i***) RGB image, (***ii***) corresponding thermal image.

2.1.2. Acquisition Protocol

As illustrated in Figure 2, before each image acquisition, each participant signed an informed consent form and was asked to remove their socks and shoes. After a 15-min acclimatization period to allow foot temperature to stabilize, the participant lay down on a stretcher, positioning their feet vertically at the end, spaced 10 cm apart. A thermal image was then captured freehandedly, without the use of any background-homogenizing object, covering both feet and the forehead simultaneously using a Samsung Galaxy S8 equipped with a FLIR ONE Pro camera [21].

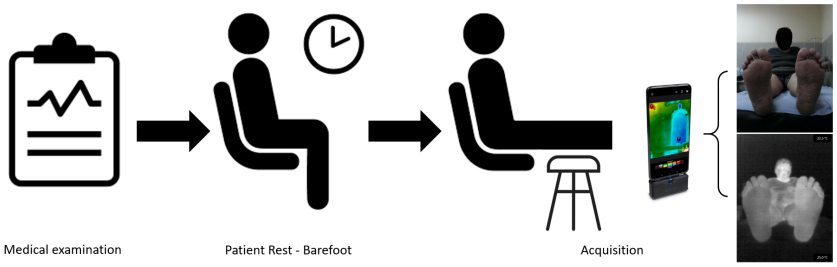


Figure 2. Acquisition protocol.

2.2. Segmentation of Regions of Interest

Segmentation consists of isolating one or more regions of interest from the background of an image to perform an analysis on relevant areas. In the medical field, this technique is widely used to extract anatomical or pathological structures from different medical images. First, two traditional methods were implemented as baselines (Adaptive Thresholding and Region Growing) to set a reference performance level. Second, five advanced encoder-decoder deep learning models (UNet, UNet ++, SegNet, DE-ResU-Net and DE-ResU-Net++) were evaluated; such architectures have proven particularly effective for medical

image segmentation with limited datasets [22–24], as in our study. The primary objective of all methods was the accurate segmentation of the plantar foot and forehead area in thermal images.

2.2.1. Traditional Baseline Methods

- Adaptive Thresholding

Adaptive Thresholding is a traditional intensity-based segmentation method that relies on the application of a locally adaptive Gaussian threshold. In our study, this approach was used to segment thermal images of DF patients. After intensity normalization, an adaptive gaussian threshold is calculated on a neighborhood of 151 pixels with a subtraction constant C = 3. The binary mask produced is then refined by morphological operations: a closing followed by an opening using a 9 × 9 pixel square kernel allows small holes to be filled and isolated noise to be eliminated, respectively.

- Region Growing

Region Growing is a classical segmentation method based on intensity similarity that relies on iterative expansion from seed points. In our work, this technique is implemented for the simultaneous segmentation of forehead and both foot regions in thermal images. Three seed points are automatically detected: one in the upper third and two in the lower quadrants, corresponding to the centers of mass of pixels exceeding the 85th and 80th percentiles, respectively. The region expansion is carried out with a tolerance of 10% and 4-connectivity. The resulting binary mask is refined through morphological operations using an elliptical 9 × 9 pixel kernel.

2.2.2. Deep Learning Methods

- U-Net architecture

U-Net [25] is a widely recognized deep learning architecture. It has demonstrated exceptional performance in biomedical image segmentation, even with limited data resources. As shown in Figure 3, U-Net features a characteristic 'U' shape. It comprises an encoder, which extracts spatial features from the image, and a decoder, which reconstructs the segmentation map. The encoder consists of four 3 × 3 convolutional blocks, each followed by 2 × 2 max pooling, doubling the number of filters with each subsampling. A bridge connects the encoder to the decoder, composed of two 3 × 3 convolutions and a 2 × 2 upsampling layer. Symmetrically, the decoder employs similar expansion blocks, combining upsampling and convolution, to produce the final segmentation map through a 1 × 1 convolution layer.

- U-Net++ architecture

U-Net++ or Nested U-Net [26] is a variant of the U-Net architecture designed to enhance segmentation accuracy by refining the skip connections between the encoder and decoder. As illustrated in Figure 4, U-Net++ introduces a series of nested, dense convolutional blocks between the corresponding levels of the encoder and decoder, thereby reducing the semantic gap between feature maps. This design improves the transfer of contextual and spatial information across the network. In addition, U-Net++ supports deep supervision, allowing segmentation maps to be generated from intermediate stages of the decoder to facilitate more efficient training.

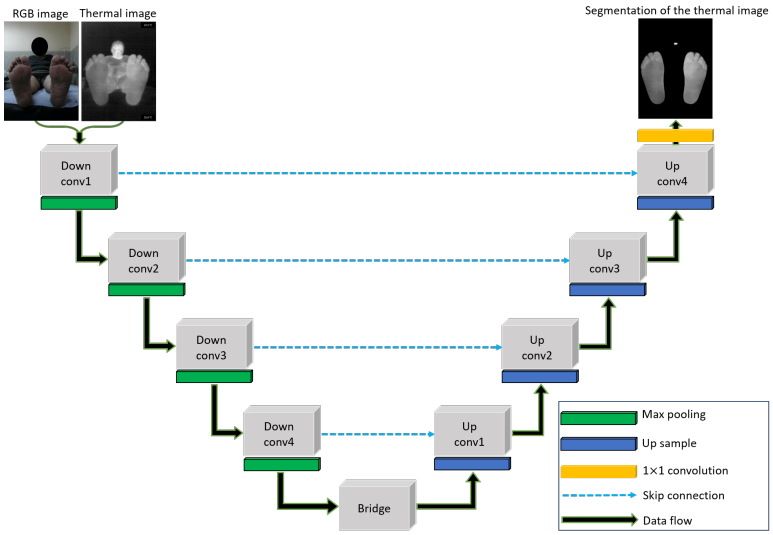


Figure 3. U-Net architecture.

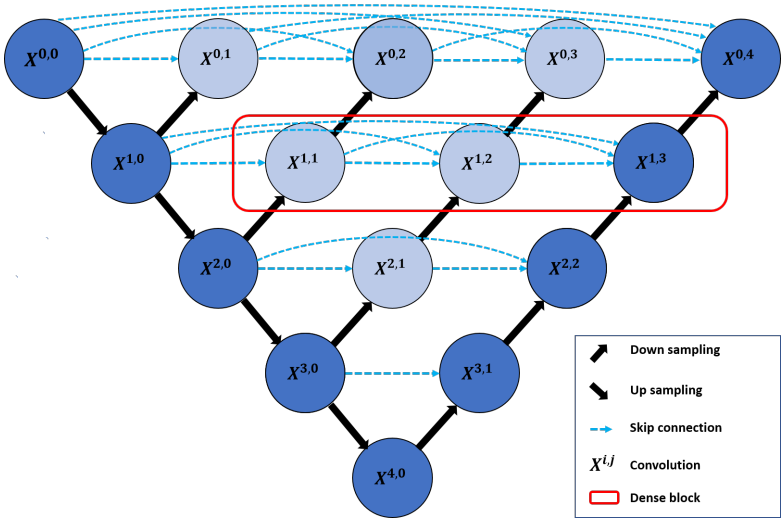


Figure 4. Dense skip connections in UNet++.

- SegNet architecture

SegNet [27] is an image segmentation architecture based on a convolutional encoder-decoder scheme. The encoder consists of successive blocks combining convolution, batch normalization, and ReLU activation function, followed by pooling layers that progressively reduce the spatial resolution while extracting discriminative features. During this step, the indices from the pooling are recorded. The decoder then reconstructs the segmentation map by applying upsampling based on these indices, ensuring better preservation of spatial information. The decoder blocks also combine convolution, normalization, and ReLU to refine the reconstructed feature maps. Finally, a softmax classification layer generates the final segmentation map.

- DE-ResUnet architecture

DE-ResUNet (Double Encoder Residual U-Net) [28], is an advanced neural architecture developed for bispectral image segmentation. It enables the integration of information from two distinct spectral domains. It is based on the principles of U-Net [25], ResNet [29], and multispectral fusion networks such as FuseNet [30] and MFNet [31]. The model follows an encoder–decoder framework and incorporates two separate encoders, each of which is dedicated to one spectral modality, to extract complementary feature representations. Both

encoders rely on modified ResNet blocks optimised for bispectral processing. The resulting feature maps are fused by concatenation and then fed into a decoder with a structure that mirrors that of the encoders. This decoder gradually reconstructs the spatial resolution while maintaining fine details through skip connections that link the encoders to the decoder. Finally, a 1 × 1 convolution layer generates the final segmentation map (see Figure 5).

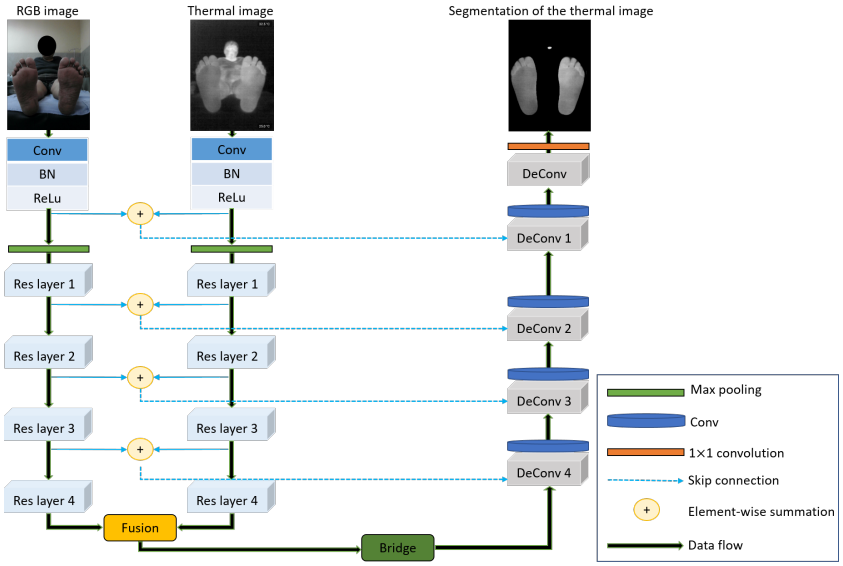


Figure 5. DE-ResUnet architecture.

- DE-ResUnet++ architecture

DE-ResUNet++ is our newly proposed architecture designed to enhance segmentation efficiency while preserving the fundamental principles of DE-ResUNet [28]. Inspired by U-Net++ [26], it incorporates dense skip connections (see Figure 4) between the two encoders and decoder layers to reduce the semantic gap between the feature levels and progressively refine the representations. Similarly to DE-ResUNet, it employs two independent encoders, each dedicated to a specific image spectrum, whose extracted features are merged by concatenation before being passed to a nested decoder. This decoder reconstructs the segmentation map through multiple intermediate sub-levels, facilitating better contextual information propagation. The architecture also integrates deep supervision, producing several outputs at different depths to stabilize the training process. Finally, a 1 × 1 convolutional layer aggregates multi-level information to generate the final segmentation map (see Figure 6).

2.3. Correction of Foot Temperatures

In this section, we present the approach used to correct foot temperatures in thermal images. As described in Section 2.1.2, each participant underwent thermal imaging that included both feet and the forehead. The forehead is used as an internal physiological temperature reference, a strategy employed to mitigate the absolute error of the FLIR One Pro camera and enhance thermal analysis. The choice of the forehead is motivated by its established reliability as a stable anatomical reference in medical thermography [19,20], its preserved vasculature in DF patients, and its practical accessibility, allowing simultaneous capture with the plantar region without additional patient manipulation. To calculate this reference temperature, we selected the 20 hottest pixels in the segmented forehead region. By focusing on the hottest pixels, we minimize the potential influence of other parts of

the segmented region on the calculation. The plantar temperature correction is then made according to Equation (1).

$$T_{\text{corrected}} = T_{\text{forehead}} - T_{\text{foot}} \quad (1)$$

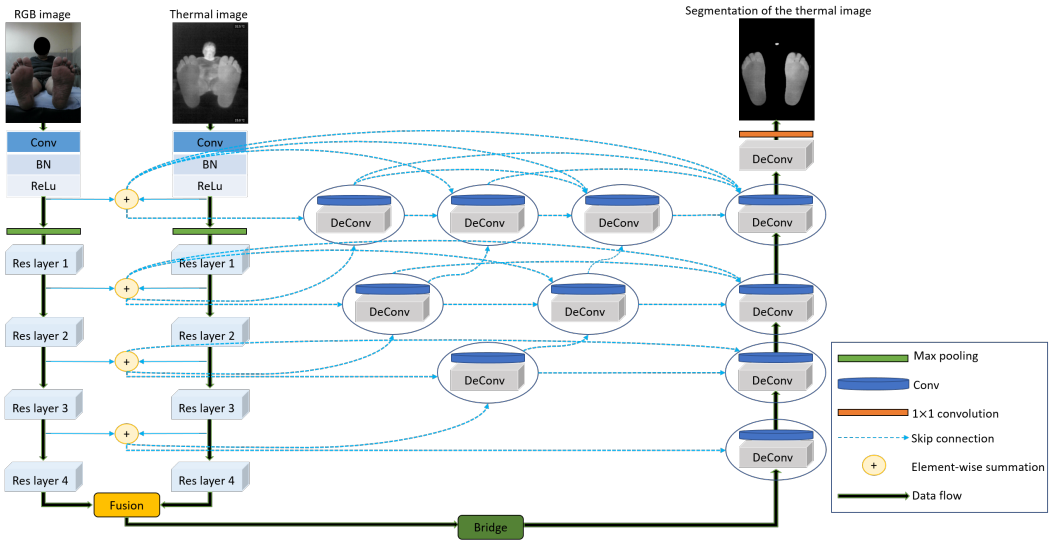


Figure 6. DE-ResUnet++ architecture.

2.4. Statistical Analyses

Descriptive statistics, including the mean, standard deviation and variance were first calculated to summarize the data. To assess the impact of the temperature correction, F-tests were applied to compare variances before and after correction. Group differences between DF patients ($n = 129$) and healthy controls ($n = 20$) were evaluated using the Mann–Whitney U test, chosen due to the unequal group sizes. To quantify the magnitude of these differences independent of sample size, Cliff's Delta (δ) was calculated as the effect size. All analyses were conducted in Python 3.12.12 using the SciPy and NumPy libraries, and statistical significance was considered at $p < 0.05$.

3. Dataset and Evaluation of Segmentation Architectures

3.1. Dataset and Training

A total of 298 pairs of thermal and RGB images of DF patients and healthy controls are included in our database, which were acquired freehandedly using the FLIR ONE Pro thermal camera. In each image, two regions of interest are clearly visible: the plantar foot and the forehead. These images were saved in PNG format and manually segmented using the MATLAB R2020a Image Labeler App [32] to generate pixel-wise ground truth masks. The annotation was performed by a trained researcher in consultation with a medical expert to ensure anatomical accuracy. Two distinct classes for segmentation were defined: one for the regions of interest (plantar foot and forehead area) and another for the background (see Figure 7). The resolution of the images is 480 × 640 pixels.

The training and evaluation of all architectures were conducted on Google Colaboratory, a cloud service providing free GPU acceleration. All experiments were implemented in Python using the PyTorch 2.9.0 library, leveraging the provided T4 GPU for computation. The data set was split into 70% for training, 10% for validation, and 20% for testing. In addition, data augmentation was applied to the training set to generate more examples and mitigate the risk of overfitting. The augmentation pipeline included random rotations ($\pm 10°$), horizontal and vertical flipping, random scaling (zoom-out in the range [0.9, 1.0]), and random variations in contrast ($\pm 10\%$) and Gaussian noise. A total of 2080 images were used.

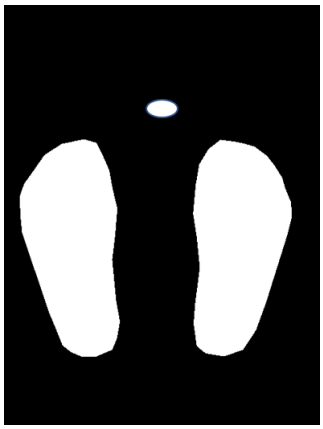


Figure 7. Ground truth of images in Figure 1.

The authors trained each model with the Adam optimizer, setting the learning rate to 0.0001 and the batch size to 4. Each network was trained until it converged over a total of 100 epochs. During training, a combination of Dice loss and binary cross-entropy was used, with deep supervision applied where relevant. Two-step gradient accumulation was performed to stabilize training with this small batch size. Validation was performed at the end of each epoch, using test time augmentation with horizontal, vertical, and combined flips. The learning rate was adjusted using a ReduceLROnPlateau scheduler based on the validation Dice score. Early stopping with a patience of 20 epochs was implemented to prevent overfitting. The model with the best performance according to the Dice validation score was saved during training.

3.2. Evaluation Metrics

To evaluate the performance of the architectures used in this study, we used three widely recognized metrics in the field of semantic segmentation: accuracy per class (Acc), Dice score (DS), and Intersection over Union (IoU). The average values of these metrics, computed across all classes, are referred to as mAcc (Equation (2)), mDS (Equation (3)), and mIoU (Equation (4)):

$$mAcc = \frac{1}{N}\sum_{i=1}^{N}\frac{TP_i}{TP_i + FN_i} \tag{2}$$

$$mDS = \frac{1}{N}\sum_{i=1}^{N}\frac{2TP_i}{2TP_i + FP_i + FN_i} \tag{3}$$

$$mIoU = \frac{1}{N}\sum_{i=1}^{N}\frac{TP_i}{TP_i + FP_i + FN_i} \tag{4}$$

where N is the total number of classes, TP_i represents the true positives for class i, FP_i the false positives, and FN_i the false negatives.

3.3. Comparative Results

3.3.1. Comparison with Traditional Segmentation Methods

To demonstrate the advantages of deep learning over classical computer vision approaches, we compare our DE-ResUNet++ architecture with two widely used traditional methods: Adaptive Thresholding and Region Growing. As shown in Table 1, traditional methods exhibit significantly lower performance compared to all deep learning architectures, with a mean Dice coefficient of 58.14% for Adaptive Thresholding and 48.30% for Region Growing, vs. 98.46% for our DE-ResUNet++. This substantial gap highlights the limitations of classical approaches for plantar foot segmentation in thermal images. These limitations are visually illustrated in Figure 8, which shows that even in optimal cases,

traditional methods suffer from over-segmentation, failure to separate adjacent structures, and excessive sensitivity to intensity variations. These limitations underscore the necessity for advanced, data-driven solutions.

Table 1. Comparison of segmentation performance (%) across different methods.

Method	Background			Regions of Interest			Mean		
	Acc	Dice	IoU	Acc	Dice	IoU	mAcc	mDice	mIoU
Thresholding	62.83	68.97	55.47	62.83	47.30	31.87	62.83	58.14	47.67
Region Growing	52.94	54.27	45.32	52.94	42.32	30.29	52.94	48.30	43.67
UNet	98.83	99.26	98.53	98.83	97.12	94.42	98.83	98.19	96.47
UNet++	98.85	99.27	98.55	98.85	97.16	94.48	98.85	98.21	96.52
SegNet	98.82	99.25	98.51	98.82	97.13	94.42	98.82	98.19	96.47
DE-ResUNet	98.99	99.36	98.73	98.99	97.51	95.16	98.99	98.43	96.94
DE-ResUNet++	99.00	99.37	98.74	99.00	97.55	95.23	99.00	98.46	96.99

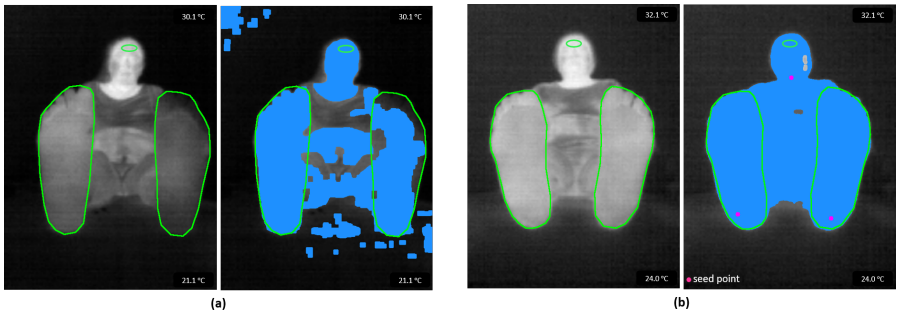


Figure 8. Representative examples showing limitations of traditional methods under optimal conditions: (**a**) Adaptive Thresholding, (**b**) Region Growing. The green line represents the ground truth mask. Blue shade indicates regions predicted by the method.

3.3.2. Comparison Among Deep Learning Architectures

Following the demonstration of deep learning superiority over traditional methods, we conduct a detailed comparison within the deep learning paradigm. We compare our new DE-ResUNet++ architecture with the DE-ResUNet, UNet, UNet++, and SegNet models. UNet, UNet++, and SegNet architectures were originally designed to process three-channel RGB images. To ensure a proper comparison with approaches that utilize multimodal data, we trained these architectures on four-channel RGB-thermal images obtained by stacking the three RGB channels with the corresponding thermal channel. The input layers of these networks were modified accordingly to accommodate this new four-channel configuration. For both DE-ResUNet and DE-ResUNet++ architectures, we adopted pre-trained ResNet-50 as the basis for both encoders, in line with the approach described in [28]. This choice aims to leverage the advantages of transfer learning, thereby reducing training time and improving the overall stability and performance of the models. Figure 9 show an example of the input images (thermal and RGB) and the predictions obtained by all networks.

Table 1 presents a quantitative comparison of the performance of the evaluated segmentation models. Conventional architectures, such as UNet, UNet++, and SegNet, demonstrated good overall performance, with an average Dice coefficient of approximately 98.2% and an average IoU close to 96.5%. However, these single-encoder models have limitations in preserving fine spatial structures, particularly at the level of the plantar contours. Figure 10 illustrates an example where these architectures did not correctly segment the toe region, unlike DE-ResUNet and DE-ResUNet++, which produced more accurate results, confirming the value of separating the encoders dedicated to thermal and RGB modalities.

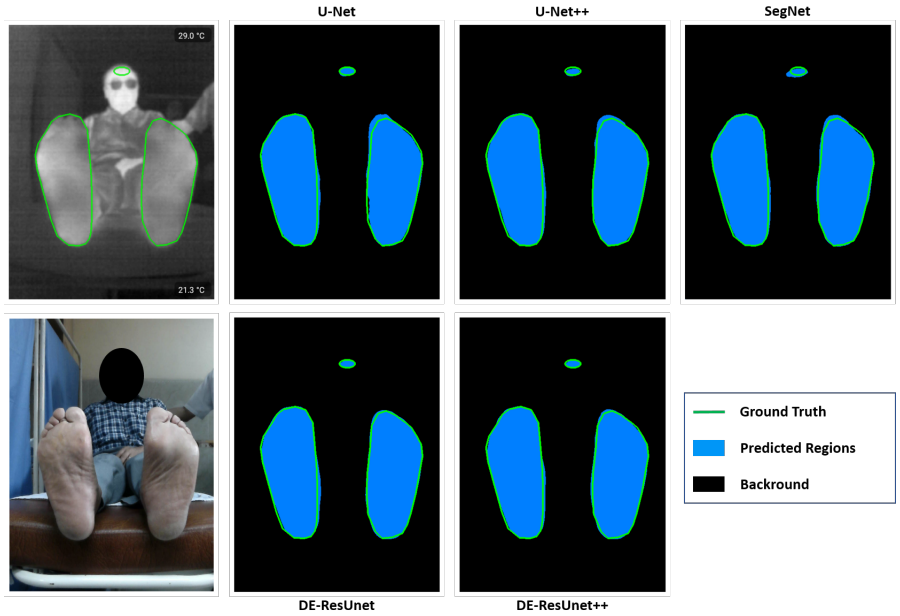


Figure 9. Representative example showing the input images (thermal and RGB) and the predictions obtained by all networks. The green line represents the ground truth mask.

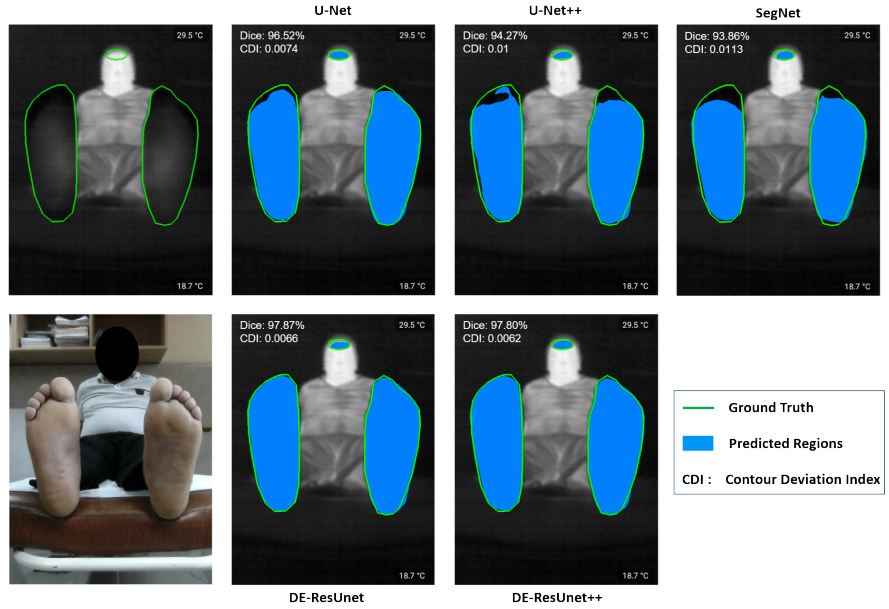


Figure 10. Representative example showing the robustness of DE-ResUNet and DE-ResUNet++ in accurately delineating fine details of the regions of interest.

A more in-depth analysis highlights the consistent superiority of DE-ResUNet++ over DE-ResUNet across all evaluation metrics (see Table 1), validating the contribution of dense connections between encoders and decoders. Figure 11 shows that DE-ResUNet++ effectively preserves interdigital separation and peripheral contours of the feet, while being more resistant to low thermal contrast and noise. Furthermore, Figure 12 illustrates its increased robustness when segmenting the frontal region, where DE-ResUNet++ generates more stable and anatomically consistent mask. These results confirm the generalization ability of DE-ResUNet++, making it particularly suitable for the thermal analysis proposed in this study.

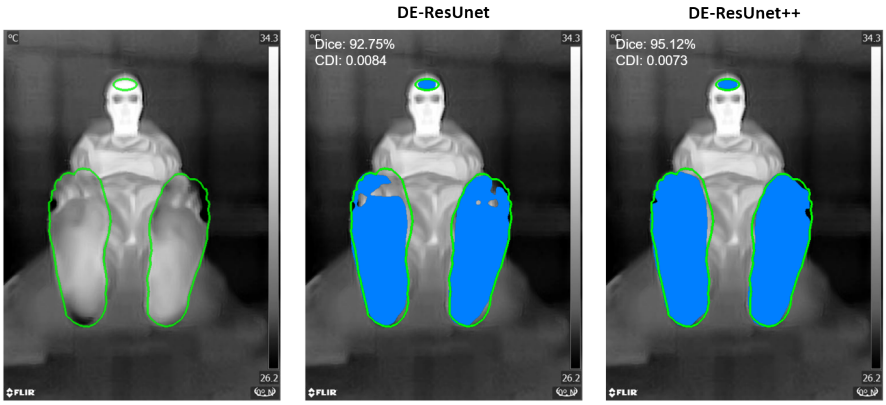


Figure 11. Example in which DE-ResUnet++ is able to segment the plantar foot compared to DE-ResUnet. The green line represents the ground truth mask; the blue shaded area shows the model's prediction.

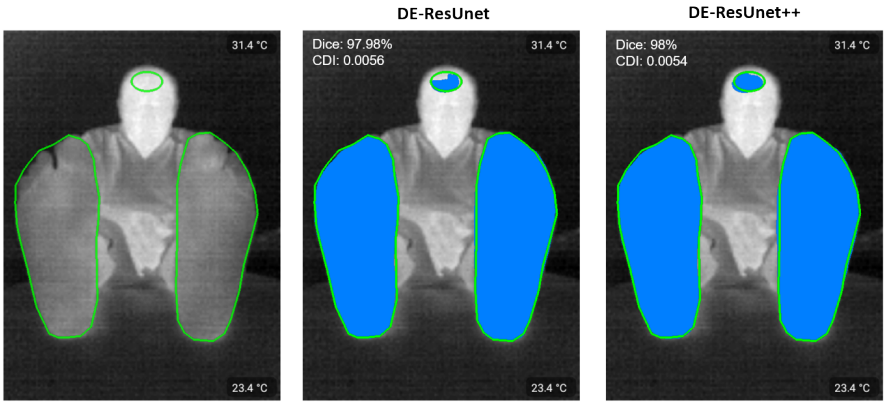


Figure 12. Example in which DE-ResUnet++ is able to segment the forehead area compared to DE-ResUnet. The green line represents the ground truth mask; the blue shaded area shows the model's prediction.

Table 2 presents the inference speed and architectural complexity of the evaluated models. SegNet achieved the fastest inference time (34.39 ms) thanks to its simple and shallow design, while UNet also demonstrated good efficiency with moderate complexity (36.52 ms). UNet++ had a much higher computational cost (102.92 ms) due to its dense connections between the encoding and decoding blocks. The dual encoder models, DE-ResUNet (55.60 ms) and DE-ResUNet++ (73.48 ms), show intermediate performance. In DE-ResUNet++, the gradual reduction in the number of channels in the deep layers lightens the computational load while preserving essential discriminative features.

Table 2. Inference speed comparison across different architectures. The inference time (ms) represents the time cost in milliseconds, and FPS represents Frames Per Second.

Architectures	Time (ms)	FPS	Parameters (M)
UNet	36.52	27.38	7.766
UNet++	102.92	9.72	9.164
SegNet	34.39	29.08	15.629
DE-ResUNet	55.60	17.98	52.955
DE-ResUNet++	73.48	13.61	54.485

3.3.3. Comparison on the Thermal Correction

To explicitly link the segmentation step to the correction application, the models are here evaluated based on their efficacy within the thermal correction procedure. Table 3

shows that all models yield a significant difference between DF patients and healthy controls groups ($p < 0.01$). However, notable variations are observed: our DE-ResUNet++ model consistently exhibits the lowest p-values and the highest AUC for both feet, distinguishing it as the most performant architecture. This analysis thereby establishes a direct and quantified link between segmentation quality and the efficacy of the thermal correction, validating the selection of DE-ResUNet++ for the subsequent stages of the study.

Table 3. Comparison of segmentation methods within the thermal correction pipeline.

Model	Right Foot		Left Foot	
	p-Value	AUC (%)	*p*-Value	AUC (%)
UNet	0.0063	69.10	0.0065	68.80
UNet++	0.0077	68.60	0.0080	68.30
SegNet	0.0077	68.60	0.0082	68.10
DE-ResUNet	0.0067	68.90	0.0069	68.70
DE-ResUNet++	0.0026	71.00	0.0025	71.10

3.3.4. Comparison Among DF Patients and Healty Controls

In this section, we compare the segmentation performance of our DeResUnet++ architecture between DF patients and healthy controls. Our model, trained on randomly shuffled data containing both groups, achieves nearly identical mDice coefficients (DF patients: 98.47%, Healthy controls: 98.39%) as shown in Table 4. The marginal 0.08% difference between groups is attributable to the class imbalance in our dataset. The near-perfect equivalence in segmentation metrics demonstrates that our method performs consistently across both populations, with performance differences negligible enough to confirm the absence of group-specific bias.

Table 4. Comparison of segmentation performance (%) by the DeResUnet++ archetecture between DF patients and healthy controls.

Group	Background			Regions of Interest			Mean		
	Acc	Dice	IoU	Acc	Dice	IoU	mAcc	mDice	mIoU
DF patients	99.01	99.38	98.75	99.01	97.56	95.24	99.01	98.47	97.00
Healthy	98.96	99.29	98.68	98.96	97.49	95.17	98.96	98.39	96.93

4. Application to Diabetic Plantar Foot

4.1. Subjects

After obtaining ethical approval from the HNDM Biomedical Research Ethics Committee (No. 075-2021-CEIB-HNDM) on 10 January 2019, a recruitment campaign was conducted in the diabetes department of the Dos de Mayo National Hospital (HNDM) in Lima, Peru. A total of 129 patients with type II diabetes (61 men and 68 women; mean age 61 ± 10.4 years) and 20 healthy control subjects (11 men and 9 women; mean age 52.1 ± 12.7 years) agreed to participate in this study. Inclusion criteria for DF patients included a confirmed diagnosis of type II diabetes and the ability to provide informed consent, while exclusion criteria included the presence of active foot ulcers, neurodegenerative diseases, or foot amputations. All participants underwent a comprehensive clinical evaluation of DF status performed by specialized physicians, as well as thermal imaging following the protocol described in Section 2.1.2, including a 15-min resting period prior to acquisition to ensure thermal stabilization.

4.2. Results

Following the comparative analysis presented in Section 3.3, we demonstrated that our DE-ResUNet++ architecture is the most effective for both segmentation and thermal correction processes. Based on this architecture, quantitative temperature analyses were performed. Table 5 ummarizes the temperature statistics (mean, SD and variance) for both feet in the healthy and DF groups, before and after thermal correction.

Table 5. Mean (°C), standard deviation (SD), and variance (Var) of right and left foot temperatures in healthy controls and DF groups, before and after the correction approach.

	Healthy Controls				**Diabetic Foot**			
	Before Correction		**After Correction**		**Before Correction**		**After Correction**	
	Right	**Left**	**Right**	**Left**	**Right**	**Left**	**Right**	**Left**
Mean	28.75	28.53	3.38	3.60	28.01	27.93	2.34	2.41
SD	1.81	1.76	1.35	1.65	1.97	2.02	1.32	1.36
Var	3.29	3.11	1.84	2.74	3.89	4.08	1.75	1.85

4.2.1. Variance Reduction

As seen in Table 5, the variance of the corrected temperatures is about twice as low as the original ones. To confirm that an F-test was applied to plantar foot temperatures before and after correction to assess whether there were significant differences between the variances. As shown in Table 6, a highly significant difference ($p < 0.01$) was observed, indicating that the correction approach effectively reduced the variability of the measured temperatures. This decrease in variance confirms the ability of the proposed method to improve the consistency of thermal data by compensating for absolute camera errors and inter-individual variations.

Table 6. F-test results comparing foot temperature variances before and after the correction approach for the whole study group.

	Right Foot	**Left Foot**
F-value	2.05375	1.87737
p-value	7.64×10^{-6}	7.41×10^{-5}

4.2.2. Improved Group Discrimination

A Mann-Whitney U test was performed to assess differences between the two groups (healthy controls and DF patients). As shown in Table 7, no significant differences were observed between the two groups when considering absolute temperatures ($p > 0.05$). However, corrected temperatures showed highly significant differences between groups ($p < 0.01$). The effect size, measured using Cliff's Delta, was $\delta = -0.420$, indicating a medium effect. These results suggest that corrected temperature may be a relevant factor in the classification and differentiation of healthy subjects and DF patients.

Table 7. Mann-Whitney U test results comparing healthy controls and DF groups, before and after the correction approach.

	Before Correction		**After Correction**	
	Right Foot	**Left Foot**	**Right Foot**	**Left Foot**
Mann-Whitney U	1000.5	1083.5	748.0	745.5
p-value	0.0684	0.1688	0.0026	0.0025
Cliff's Delta (δ)	−0.253	−0.191	−0.420	−0.422

4.2.3. Group-Specific Correction Effects

Analysis of Table 5 reveals differential effects of the correction across groups. DF patients exhibit greater variance reduction than healthy controls (55% vs. 44%). The standard deviation also decreases more substantially in DF patients (1.97 to 1.32 compared to 1.81 to 1.35 in healty controls). Following correction, both groups reach a similar temperature range (2.34–3.38 °C) while retaining inter-group differences. This differential reduction suggests that the correction is more effective on the initially more heterogeneous temperatures of diabetic feet.

5. Discussion

This study aimed to develop a new thermal correction strategy using the forehead as an internal thermal reference, in order to address the fundamental limitations of mobile thermography using smartphones.

Our approach specifically addresses the challenges posed by the emergence of infrared smartphone cameras. Although the literature notes the growing use of these devices [33–36], but highlights their resolution limitations and inability to accurately measure absolute temperatures [34,37], our thermal correction method offers an innovative solution. While studies [34,35,37] use contralateral foot comparison for relative assessment, our work introduces a paradigm shift by proposing an active correction of the absolute error, exploiting the forehead as a stable internal reference [38].

This correction strategy is part of a comprehensive approach that aims to simplify image acquisition while ensuring its reliability. Unlike other studies, such as [39,40], which impose strictly standardized acquisition conditions such as background homogenization and reflective environment control, our method has been designed to be free of restrictive protocols. This feature accurately reproduces real-world conditions of use, both in clinical practice and for self-monitoring at home. The robustness of our approach also lies in its fully automated nature, eliminating sources of error related to human intervention. By exploiting our robust DE-ResUNet++ architecture with a Dice score of 98.46%, we ensure reproducible segmentation of regions of interest while guaranteeing perfect standardization of measurements.

Results demonstrate the relevance of our approach. The significant reduction in thermal variance after the correction approach confirms that our method allows for data harmonization. In particular, the ability of corrected temperatures to distinguish DF patients from healthy controls, unlike absolute values, is a remarkable finding. This result sheds new light on the contradictions in the literature. Although our study, like those of [41–43], measures lower plantar foot temperatures in DF patients compared to healthy controls, other studies [33,44–46] observe the opposite effect. Given these inconsistencies, a thermal correction method is, therefore, essential. The strength of our method is that it provides a reliable and reproducible measurement capable of revealing the actual thermal signal, beyond these measurement artifacts.

This result is consistent with the observations in [35], which suggested that smartphone images could be sufficient for data comparison when properly processed. Thus, our method reveals thermal signals that were masked by instrumental error, offering a new perspective for the early detection of complications [47–49]. Unlike approaches based on angiosomes [12,50], where there is a lack of consensus, our method provides a reproducible and standardized measurement. In addition, and as conceptually summarized in Table 8, our correction strategy offers a robust alternative to the contralateral comparisons used in [34,47,51,52] . However, these approaches assume that one foot can serve as a healthy control for the other, a fragile assumption given the systemic nature of DF and the high

prevalence of comorbidities [36,50,53]. Our method, by avoiding this assumption, is therefore more reliable in a real clinical context.

Table 8. Conceptual comparison between our method and the contralateral reference method.

Aspect	Contralateral Reference Method	Proposed Method
Basic Principle	Relative comparison: affected foot vs. contralateral foot.	Absolute correction: foot temperature corrected by a stable internal reference (forehead).
Reference Standard	Assumes the contralateral foot is a healthy control.	Uses the forehead, a region independent of foot pathology.
Handles Bilateral Involvement	Problematic. Loses validity if both feet are affected.	Robust. Applicable regardless of foot condition.
Compensates for Sensor Error	No. Relies on error cancellation between feet.	Yes. Actively corrects the sensor's absolute error via differential measurement.
Primary Output	ΔT contralateral (single value).	Corrected temperature (forehead reference, per foot).
Clinical Application	Detection of asymmetry.	Standardized thermometry for screening and longitudinal tracking.

It is also important to consider the sensor's inherent characteristics. The proposed differential measurement inherently mitigates the impact of global calibration drift (Equation (1)). Furthermore, spatial averaging over the segmented regions reduces the influence of random sensor noise on the mean temperatures. These design choices help ensure the robustness of the corrected thermal measurements despite the limitations of the consumer-grade thermal imager used.

The main limitations are similar to those identified in the literature. As highlighted in studies [34,37], the characteristics of the camera influence the results. Although our method corrects for absolute error, its validation with a wide range of smartphone cameras, particularly which are promising in terms of accessibility [33–36], remains to be confirmed. The development of a mobile application integrating our correction algorithm, in line with initiatives such as [33,54], would represent a major step forward in prevention. The creation of a large thermographic database, as suggested by other authors [53], would be a major step toward establishing robust standards.

By offering a robust solution for correcting the absolute error of cameras and automating analysis, our method represents a significant step forward in standardizing medical thermography. Its validation on a larger scale, on more diverse cohorts, could make it a valuable tool for the early detection of DF complications, meeting the need for reliable and reproducible methods.

6. Conclusions and Perspectives

In this study, the main objective was to develop a new strategy to correct foot temperatures in thermal images by avoiding the significant absolute error of the thermal camera and improving thermal analysis. We introduced a physiologically motivated two-region segmentation (forehead + plantar foot) to enable stable temperature correction for smart-

phone thermal imaging. This work relied on a new multimodal thermal–RGB dataset annotated in detail. A fully automated joint method was developed for segmentation. Among the five deep learning architectures tested and compared against traditional methods, our DE-ResUnet++ provided the best performance (Dice score: 98.46%). A clinical study verifies that the correction method significantly reduces temperature variance and enhances discrimination between DF patients and healthy controls. These findings suggest the validity of our proposed approach for improving mobile thermal imaging capabilities, carrying important clinical potential for DF complication prevention. As a perspective, this method will need to be validated on larger and more diverse cohorts before integration into clinical practice.

Author Contributions: Conceptualization, H.E. and R.H.; methodology, H.E., R.H. and H.D.; software, H.E. and A.A.; validation, H.E., R.H. and I.D.; formal analysis, H.E.; investigation, H.E., A.A. and I.D.; resources, R.H., H.D. and I.D.; data curation, H.E. and A.A.; writing—original draft preparation, H.E.; writing—review and editing, R.H., H.D. and A.A.; visualization, H.E.; supervision, R.H. and H.D.; project administration, R.H.; funding acquisition, R.H. and H.D. All authors have read and agreed to the published version of the manuscript.

Funding: This research received no external funding.

Institutional Review Board Statement: The study was conducted in accordance with the Declaration of Helsinki, and approved by the Biomedical Research Ethics Committee of Hospital Nacional Dos De Mayo (protocol code 075-2021-CEIB-HNDM, date of approval 10 January 2019).

Informed Consent Statement: All participants provided informed consent before taking part in the study.

Data Availability Statement: The data presented in this study are available on request from the corresponding author. The images containing facial data are not publicly available due to privacy restrictions.

Acknowledgments: The authors thank the European STANDUP project (Horizon 2020, Grant Agreement No. 777661) for providing the dataset used in this study. We also thank the clinical team at Hospital Nacional Dos De Mayo and all participating patients.

Conflicts of Interest: The authors declare no conflicts of interest. The funders had no role in the design of the study; in the collection, analyses, or interpretation of data; in the writing of the manuscript; or in the decision to publish the results.

References

1. Deshpande, A.D.; Harris-Hayes, M.; Schootman, M. Epidemiology of diabetes and diabetes-related complications. *Phys. Ther.* **2008**, *88*, 1254–1264. [CrossRef] [PubMed]
2. Harding, J.L.; Pavkov, M.E.; Magliano, D.J.; Shaw, J.E.; Gregg, E.W. Global trends in diabetes complications: A review of current evidence. *Diabetologia* **2019**, *62*, 3–16. [CrossRef] [PubMed]
3. Van Netten, J.J.; Bus, S.A.; Apelqvist, J.; Lipsky, B.A.; Hinchliffe, R.J.; Game, F.; Rayman, G.; Lazzarini, P.A.; Forsythe, R.O.; Peters, E.J.G.; et al. Definitions and criteria for diabetic foot disease. *Diabetes Metab. Res. Rev.* **2020**, *36*, e3268. [CrossRef] [PubMed]
4. Mishra, S.C.; Chhatbar, K.C.; Kashikar, A.; Mehndiratta, A. Diabetic foot. *BMJ* **2017**, *359*, j5064. [CrossRef]
5. Armstrong, D.G.; Tan, T.-W.; Boulton, A.J.M.; Bus, S.A. Diabetic foot ulcers: A review. *JAMA* **2023**, *330*, 62–75. [CrossRef]
6. Lo, Z.J.; Surendra, N.K.; Saxena, A.; Car, J. Clinical and economic burden of diabetic foot ulcers: A 5-year longitudinal multi-ethnic cohort study from the tropics. *Int. Wound J.* **2021**, *18*, 375–386. [CrossRef]
7. Armstrong, D.G.; Holtz-Neiderer, K.; Wendel, C.; Mohler, M.J.; Kimbriel, H.R.; Lavery, L.A. Skin temperature monitoring reduces the risk for diabetic foot ulceration in high-risk patients. *Am. J. Med.* **2007**, *120*, 1042–1046. [CrossRef]
8. Lavery, L.A.; Higgins, K.R.; Lanctot, D.R.; Constantinides, G.P.; Zamorano, R.G.; Armstrong, D.G.; Athanasiou, K.A.; Agrawal, C.M. Home monitoring of foot skin temperatures to prevent ulceration. *Diabetes Care* **2004**, *27*, 2642–2647. [CrossRef]
9. Ammer, K.; Melnizky, P.; Rathkolb, O.; Ring, E.F. Thermal imaging of skin changes on the feet of type II diabetics. In Proceedings of the 23rd Annual International Conference of the IEEE Engineering in Medicine and Biology Society, Istanbul, Turkey, 25–28 October 2001; Volume 3, pp. 2870–2872.

10. Kaabouch, N.; Chen, Y.; Hu, W.-C.; Anderson, J.W.; Ames, F.; Paulson, R. Enhancement of the asymmetry-based overlapping analysis through features extraction. In Proceedings of the SPIE Conference on Electronic Imaging, San Francisco, CA, USA, 23–27 January 2011; p. 013012.
11. Kaabouch, N.; Hu, W.-C.; Chen, Y. Alternative technique to asymmetry analysis-based overlapping for foot ulcer examination: Scalable scanning. *arXiv* **2016**, arXiv:1606.03578. [CrossRef]
12. Elfahimi, H.; Bouallal, D.; Douzi, H.; Harba, R.; Boujerfaoui, S. AI and Angiosome Based Analysis of Diabetic Foot Thermal Images for the Diagnosis of Ulcer Risk. In Proceedings of the IEEE Thirteenth International Conference on Image Processing Theory, Tools and Applications, Paris, France, 4–7 November 2024; pp. 1–4.
13. Bharara, M.; Viswanathan, V.; Cobb, J.E. Cold immersion recovery responses in the diabetic foot with neuropathy. *Int. Wound J.* **2008**, *5*, 562–569. [CrossRef]
14. Chekh, V.; Soliz, P.; Burge, M.; Luan, S. A physiological thermal regulation model with application to the diagnosis of diabetic peripheral neuropathy. In Proceedings of the 8th ACM International Conference on Bioinformatics, Computational Biology, and Health Informatics, Boston, MA, USA, 20–23 August 2017; pp. 544–549.
15. FLIR. Flir One Pro Thermal Imaging Camera for Smartphones. Available online: https://www.flir.com/products/flir-one-pro/ (accessed on 22 April 2025).
16. TESTOON. Hikmicro Mini 1 Thermal Camera for Smartphone/Tablet. Available online: https://www.testoon.com/shop/hikmini1-mini-1-41302 (accessed on 22 April 2025).
17. UNI-T. Uti721m Smartphone Thermal Camera Module for Android. Available online: https://teams.microsoft.com/l/message/19:067831cb-e3e3-4bf8-a23d-c5d4a1413902_d30c8081-7cda-4fd9-8268-f5dd9084607c@unq.gbl.spaces/1769393884096?context=%7B%22contextType%22%3A%22chat%22%7D (accessed on 22 April 2025).
18. TOPDON. Tc001 for Android. Available online: https://topdon-france.com/produit/tc-001/ (accessed on 22 April 2025).
19. Fernández-Cuevas, I.; Marins, J.C.B.; Lastras, J.A.; Carmona, P.M.G.; Cano, S.P.; García-Concepción, M.Á.; Sillero-Quintana, M. Classification of factors influencing the use of infrared thermography in humans: A review. *Infrared Phys. Technol.* **2015**, *71*, 28–55. [CrossRef]
20. Ring, E.F.J.; Ammer, K. Infrared thermal imaging in medicine. *Physiol. Meas.* **2012**, *33*, R33. [CrossRef]
21. Bouallal, D.; Bougrine, A.; Harba, R.; Canals, R.; Douzi, H.; Vilcahuaman, L.; Arbanil, H. STANDUP database of plantar foot thermal and RGB images for early ulcer detection. *Open Res. Eur.* **2022**, *2*, 77. [CrossRef]
22. Azad, R.; Aghdam, E.K.; Rauland, A.; Jia, Y.; Avval, A.H.; Bozorgpour, A.; Karimijafarbigloo, S.; Cohen, J.P.; Adeli, E.; Merhof, D. Medical image segmentation review: The success of u-net. *IEEE Trans. Pattern Anal. Mach. Intell.* 2024, *in press*. [CrossRef] [PubMed]
23. Siddique, N.; Sidike, P.; Elkin, C.; Devabhaktuni, V. U-Net and its variants for medical image segmentation: Theory and applications. *arXiv* **2020**, arXiv:2011.01118. [CrossRef]
24. Ehab, W.; Huang, L.; Li, Y. UNet and Variants for Medical Image Segmentation. *Int. J. Netw. Dyn. Intell.* **2024**, *3*, 100009. [CrossRef]
25. Ronneberger, O.; Fischer, P.; Brox, T. U-net: Convolutional networks for biomedical image segmentation. In Proceedings of the International Conference on Medical Image Computing and Computer-Assisted Intervention, Munich, Germany, 5–9 October 2015; pp. 234–241.
26. Zhou, Z.; Siddiquee, M.M.R.; Tajbakhsh, N.; Liang, J. Unet++: A nested u-net architecture for medical image segmentation. In Proceedings of the International Workshop on Deep Learning in Medical Image Analysis, Granada, Spain, 20 September 2018; pp. 3–11.
27. Badrinarayanan, V.; Kendall, A.; Cipolla, R. Segnet: A deep convolutional encoder-decoder architecture for image segmentation. *IEEE Trans. Pattern Anal. Mach. Intell.* **2017**, *39*, 2481–2495. [CrossRef]
28. Bouallal, D.; Douzi, H.; Harba, R. Diabetic foot thermal image segmentation using Double Encoder-ResUnet (DE-ResUnet). *J. Med. Eng. Technol.* **2022**, *46*, 378–392. [CrossRef]
29. He, K.; Zhang, X.; Ren, S.; Sun, J. Deep residual learning for image recognition. In Proceedings of the IEEE Conference on Computer Vision and Pattern Recognition, Las Vegas, NV, USA, 27–30 June 2016; pp. 770–778.
30. Hazirbas, C.; Ma, L.; Domokos, C.; Cremers, D. Fusenet: Incorporating depth into semantic segmentation via fusion-based cnn architecture. In Proceedings of the Asian Conference on Computer Vision, Taipei, Taiwan, 20–24 November 2016; pp. 213–228.
31. Ha, Q.; Watanabe, K.; Karasawa, T.; Ushiku, Y.; Harada, T. MFNet: Towards real-time semantic segmentation for autonomous vehicles with multi-spectral scenes. In Proceedings of the IEEE/RSJ International Conference on Intelligent Robots and Systems, Vancouver, BC, Canada, 24–28 September 2017; pp. 5108–5115.
32. MATLAB. Label Images for Computer Vision Applications. Available online: https://www.mathworks.com/help/vision/ref/imagelabeler-app.html (accessed on 22 April 2025).
33. Fraiwan, L.; Ninan, J.; Al-Khodari, M. Mobile application for ulcer detection. *Open Biomed. Eng. J.* **2018**, *12*, 16. [CrossRef]
34. Van Doremalen, R.F.M.; Van Netten, J.J.; Van Baal, J.G.; Vollenbroek-Hutten, M.M.R.; van der Heijden, F. Validation of low-cost smartphone-based thermal camera for diabetic foot assessment. *Diabetes Res. Clin. Pract.* **2019**, *149*, 132–139. [CrossRef]

35. Kanazawa, T.; Nakagami, G.; Goto, T.; Noguchi, H.; Oe, M.; Miyagaki, T.; Hayashi, A.; Sasaki, S.; Sanada, H. Use of smartphone attached mobile thermography assessing subclinical inflammation: A pilot study. *J. Wound Care* **2016**, *25*, 177–182. [CrossRef]
36. Oe, M.; Tsuruoka, K.; Ohashi, Y.; Takehara, K.; Noguchi, H.; Mori, T.; Yamauchi, T.; Sanada, H. Prevention of diabetic foot ulcers using a smartphone and mobile thermography: A case study. *J. Wound Care* **2021**, *30*, 116–119. [CrossRef]
37. van Doremalen, R.F.M.; van Netten, J.J.; van Baal, J.G.; Vollenbroek-Hutten, M.M.R.; van der Heijden, F. Infrared 3D thermography for inflammation detection in diabetic foot disease: A proof of concept. *J. Diabetes Sci. Technol.* **2020**, *14*, 46–54. [CrossRef]
38. Mauriz, E.; Caloca-Amber, S.; Vázquez-Casares, A.M. Effect of facial skin temperature on the perception of anxiety: A pilot study. In Proceedings of the Healthcare Conference, Basel, Switzerland, 1–30 June 2020; p. 206.
39. Fraiwan, L.; AlKhodari, M.; Ninan, J.; Mustafa, B.; Saleh, A.; Ghazal, M. Diabetic foot ulcer mobile detection system using smart phone thermal camera: A feasibility study. *Biomed. Eng. Online* **2017**, *16*, 117. [CrossRef]
40. Vilcahuaman, L.; Harba, R.; Canals, R.; Zequera, M.; Wilches, C.; Arista, M.T.; Torres, L.; Arbanil, H. Automatic analysis of plantar foot thermal images in at-risk type II diabetes by using an infrared camera. In Proceedings of the World Congress on Medical Physics and Biomedical Engineering, Toronto, Canada, 7–12 June 2015; pp. 228–231.
41. Astasio-Picado, Á.; Martínez, E.E.; Gómez-Martín, B. Comparative thermal map of the foot between patients with and without diabetes through the use of infrared thermography. *Enferm. Clin.* **2020**, *30*, 119–123. [CrossRef] [PubMed]
42. Machin, G.; Whittam, A.; Ainarkar, S.; Allen, J.; Bevans, J.; Edmonds, M.; Kluwe, B.; Macdonald, A.; Petrova, N.; Plassmann, P.; et al. A medical thermal imaging device for the prevention of diabetic foot ulceration. *Physiol. Meas.* **2017**, *38*, 420. [CrossRef] [PubMed]
43. Rai, M.; Maity, T.; Sharma, R.; Yadav, R.K. Early detection of foot ulceration in type II diabetic patient using registration method in infrared images and descriptive comparison with deep learning methods. *J. Supercomput.* **2022**, *78*, 13409–13426. [CrossRef]
44. Ilo, A.; Romsi, P.; Mäkelä, J. Infrared thermography and vascular disorders in diabetic feet. *J. Diabetes Sci. Technol.* **2020**, *14*, 28–36. [CrossRef]
45. Zhou, Q.; Qian, Z.; Wu, J.; Liu, J.; Ren, L.; Ren, L. Early diagnosis of diabetic peripheral neuropathy based on infrared thermal imaging technology. *Diabetes Metab. Res. Rev.* **2021**, *37*, e3429. [CrossRef]
46. Dębiec-Bąk, A.; Skrzek, A.; Ptak, A.; Majerski, K.; Uiberlayová, I.; Stefańska, M. Evaluation of the surface temperature distribution in the feet of patients with type 2 diabetes using the thermovision method. *Physiother. Q.* **2023**, *31*, 92–97. [CrossRef]
47. Petrova, N.L.; Donaldson, N.K.; Tang, W.; MacDonald, A.; Allen, J.; Lomas, C.; Leech, N.; Ainarkar, S.; Bevans, J.; Plassmann, P.; et al. Infrared thermography and ulcer prevention in the high-risk diabetic foot: Data from a single-blind multicentre controlled clinical trial. *Diabet. Med.* **2020**, *37*, 95–104. [CrossRef]
48. Aliahmad, B.; Tint, A.N.; Arjunan, S.P.; Rani, P.; Kumar, D.K.; Miller, J.; Zajac, J.D.; Wang, G.; Ekinci, E.I. Is thermal imaging a useful predictor of the healing status of diabetes-related foot ulcers? A pilot study. *J. Diabetes Sci. Technol.* **2019**, *13*, 561–567. [CrossRef]
49. Gethin, G.; O'Connor, G.M.; Abedin, J.; Newell, J.; Flynn, L.; Watterson, D.; O'Loughlin, A. Monitoring of pH and temperature of neuropathic diabetic and nondiabetic foot ulcers for 12 weeks: An observational study. *Wound Repair Regen.* **2018**, *26*, 251–256. [CrossRef]
50. Carabott, M.; Formosa, C.; Mizzi, A.; Papanas, N.; Gatt, A. Thermographic characteristics of the diabetic foot with peripheral arterial disease using the angiosome concept. *Exp. Clin. Endocrinol. Diabetes* **2021**, *129*, 93–98. [CrossRef] [PubMed]
51. Macdonald, A.; Petrova, N.; Ainarker, S.; Allen, J.; Lomas, C.; Tang, W.; Plassmann, P.; Whittam, A.; Bevans, J.; Ring, F.; et al. Between visit variability of thermal imaging of feet in people attending podiatric clinics with diabetic neuropathy at high risk of developing foot ulcers. *Physiol. Meas.* **2019**, *40*, 084004. [CrossRef] [PubMed]
52. van Netten, J.J.; van Baal, J.G.; Liu, C.; van Der Heijden, F.; Bus, S.A. Infrared thermal imaging for automated detection of diabetic foot complications. *J. Diabetes Sci. Technol.* 2013, *accepted*. [CrossRef] [PubMed]
53. Hernandez-Contreras, D.A.; Peregrina-Barreto, H.; de Jesus Rangel-Magdaleno, J.; Renero-Carrillo, F.J. Plantar thermogram database for the study of diabetic foot complications. *IEEE Access* **2019**, *7*, 161296–161307. [CrossRef]
54. Agustini, N.L.P.I.B.; Suniyadewi, N.W.; Rismayanti, I.D.A.; Faridah, V.N.; Utami, R.; Aris, A.; Nursalam, N. Development and validation of android based mobile app for diabetic foot early self-assessment. *Malays. J. Public Health Med.* **2022**, *22*, 95–102.

Disclaimer/Publisher's Note: The statements, opinions and data contained in all publications are solely those of the individual author(s) and contributor(s) and not of MDPI and/or the editor(s). MDPI and/or the editor(s) disclaim responsibility for any injury to people or property resulting from any ideas, methods, instructions or products referred to in the content.